Bio-Design and Manufacturing (2024) 7:428–438
https://doi.org/10.1007/s42242-024-00294-2

RESEARCH ARTICLE

A crosstalk-free dual-mode sweat sensing system for naked-eye sweat loss quantification via changes in structural reflectance

Bowen Zhong[1,2] · Hao Xu[1,2] · Xiaokun Qin[1,2] · Lingchen Liu[1,2] · Hailong Wang[1,2] · Lili Wang[1,2]

Received: 28 September 2023 / Accepted: 10 May 2024 / Published online: 11 July 2024

Abstract

Sweat loss monitoring is important for understanding the body's thermoregulation and hydration status, as well as for comprehensive sweat analysis. Despite recent advances, developing a low-cost, scalable, and universal method for the fabrication of colorimetric microfluidics designed for sweat loss monitoring remains challenging. In this study, we propose a novel laser-engraved surface roughening strategy for various flexible substrates. This process permits the construction of microchannels that show distinct structural reflectance changes before and after sweat filling. By leveraging these unique optical properties, we have developed a fully laser-engraved microfluidic device for the quantification of naked-eye sweat loss. This sweat loss sensor is capable of a volume resolution of 0.5 μL and a total volume capacity of 11 μL, and can be customized to meet different performance requirements. Moreover, we report the development of a crosstalk-free dual-mode sweat microfluidic system that integrates an Ag/AgCl chloride sensor and a matching wireless measurement flexible printed circuit board. This integrated system enables the real-time monitoring of colorimetric sweat loss signals and potential ion concentration signals without crosstalk. Finally, we demonstrate the potential practical use of this microfluidic sweat loss sensor and its integrated system for sports medicine via on-body studies.

Graphic abstract

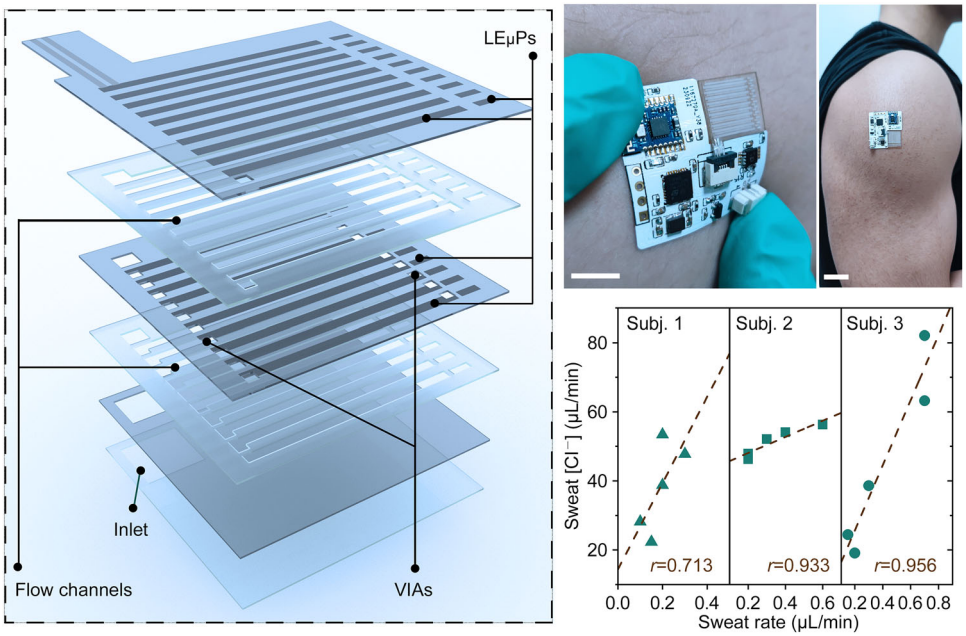

Keywords Sweat loss sensor · Microfluidic design · Structural reflectance · Dual-mode integration · Crosstalk-free

Extended author information available on the last page of the article

Introduction

Sweat sensors capable of noninvasively monitoring patient health on the molecular level have attracted significant attention in the field of wearable electronics, since they would be highly valuable for personalized and precision health care [1–4]. Recently, advanced wearable sweat sensors for continuous and real-time monitoring of biomolecules have permitted the identification of a large number of sweat components (e.g., electrolytes [5], hormones [6], amino acids [7], and proteins [8]) that can serve as biomarkers of specific physiological conditions [9, 10]. In addition to molecular-level concentration indicators, the real-time monitoring of dynamic sweat indicators (i.e., the volume and rate of sweat loss) can be important for various applications. For example, sweat dynamic indicators can provide estimates of water loss that can be used to quantitatively assess the body's thermoregulation and hydration status [11]. More importantly, the simultaneous measurement and analysis of sweat dynamics and concentration indicators can provide information regarding mechanisms of molecular partitioning and transport [12, 13] and act as a comprehensive health surveillance system for the concentrations of various sweat-soluble nutrients [14, 15]. For instance, recording individual sweat profiles during exercise and heat stress can facilitate the development of personalized fluid replacement strategies capable of improving body performance and preventing adverse conditions caused by excessive water and/or electrolyte loss [16, 17]. To do so, current research on multimodal sweat sensors involves assessing how to compatibly integrate sweat loss monitoring modules with existing biosensing technologies via new designs and scalable manufacturing technologies.

Currently, there are several wearable platforms for sweat loss quantification. These can be divided into three categories according to structure, including hygrometer-, absorbent-material-, and microfluidics-based frameworks [11, 18]. Hygrometer-based platforms are generally difficult to wear and integrate with biosensors, and therefore, we do not discuss them further in this paper. Regarding absorbent-material-based platforms, it can be convenient to collect sweat from the skin using absorbent materials for sweat loss monitoring, but associated colorimetric measurement technologies often have low resolution [19, 20], and electrical measurements can be easily affected by the electrolyte concentration of sweat samples [21]. Furthermore, these platforms cannot avoid the mixing of old and new sweat, which results in integrated biosensors being disposable and replaceable, thereby increasing cost [22]. In contrast, microfluidic devices are more suitable for both sweat loss monitoring and integration with biosensors due to their ability to continuously sample, route, and refresh microliters of sweat. In general, electrical measurements (e.g., admittance and capacitance) have notable advantages, including relatively high accuracy, high resolution, and good compatibility with electrochemical biosensors [23–29]. However, they also face unavoidable development bottlenecks caused by system complexity; these include but are not limited to electrical signal crosstalk between concentration and sweat volume signals. They also present challenges related to decoupling processes, manufacturing complexity, and difficulty in interpreting signal readouts [30].

Another microfluidics-based method involves the colorimetric measurement of sweat loss. This method shows strong user acceptance in the commercial market due to the simplicity by which sensors are manufactured as well as the fact that this method generates convenient visual readouts that can be read by the user's naked eye or a portable device [31, 32]. This method is commonly implemented using water-soluble dyes for irreversible colorimetric reactions in or near the inlet or within the microchannel. These reactions color the collected sweat front and pass a fixed volume through the flow channel [33–35]. The use of dyes has shown strong compatibility and integration with colorimetric biosensors [36–38], but dye dependence also results in irreversible contamination and depletion of the channel after first use. This makes this method disposable, and reuse requires replenishment and reassembly [39]. This reusability challenge can be effectively addressed by creating a structural color effect [40, 41], which can be achieved by roughening the surface of the flow channel to create observable differences in structural reflectance before and after sweat filling. However, the design and fabrication of sweat loss sensors based on this principle remain underdeveloped due to the scarcity of low-cost, universally applicable approaches for roughening the surface structures of microchannels. For example, existing methods generally require expensive and complex soft lithography [41] or can only be fabricated on specific substrates that can be laser-carbonized [42]. Therefore, it remains a challenge to develop a method to roughen flow channels on various flexible substrates; however, resolving this challenge would facilitate the large-scale manufacturing of microfluidics-based sweat loss sensors.

In this study, we developed a universal roughening strategy that uses a simple and low-cost laser-engraved pitting mode to ablate microscale pit arrays that are compatible with many common microfluidic substrates. Subsequent analysis of the roughened and visualized flow microchannels assembled using laser-engraved micropits (LEμPs) and laser-engraved channels showed obvious changes in structural reflectance before and after sweat filling. Based on this approach, we then designed and fabricated a fully laser-engraved colorimetric microfluidic device for naked-eye sweat loss quantification by presetting and marking the volume of each discrete flow channel. Due to its vertically and alternately assembled channel structure, this device has a volume resolution that can

vary by adjusting the width and length of the channel while maintaining a small footprint (i.e., a resolution of 0.5 μL was achieved for 11 μL of total volume over a demonstration area of 1.25 cm × 1.30 cm). By integrating this system with a chloride sensor and a matching flexible printed circuit board (FPCB), the resulting wearable microfluidic system enabled continuous and dual-mode monitoring of sweat loss and chloride concentration without complications related to crosstalk. We conducted a practical application demonstration of this design by successfully detecting differences in sweat loss levels for several subjects during exercise. Finally, we demonstrated that the integrated system is capable of real-time dual-mode sweat analysis, thereby enabling it to track the sweat profiles of individuals. We anticipate that this will be useful for sports health surveillance and management.

Methods

Materials

NaCl, $FeCl_3$, and methanol were purchased from Innochem (Beijing, China). Polyvinyl butyral (PVB), multiwall carbon nanotubes (MWCNTs), and block polymer PEO-PPO-PEO (F127) were purchased from Sigma-Aldrich (Shanghai, China). Chrome tungsten and silver wires for thermal evaporation were purchased from ZhongNuo Advanced Material (Beijing) Technology Co., Ltd. (Beijing, China). Polyethylene terephthalate (PET), polyimide (PI), and polyethylene naphthalate (PEN) were purchased from Huanan Xiangcheng Technology Co., Ltd. (Yiyang, China). Double-sided tape (100 μm thick, 7982) was purchased from Crown New Materials Technology Co., Ltd. (Zhongshan, China).

Microfluidic module fabrication

The six layers of the microfluidic module, each of which had specific patterns, were fully fabricated via laser engraving using an yttrium aluminum garnet (YAG) laser cutter (Suzhou Inngu Laser, Suzhou, China). The universal roughening strategy used for the top layer of the flow channel also relied on the laser cutter. Specifically, we used the laser-engraved pitting mode of the laser cutter to produce a patterned periodic array of ablated pits with a width of about 32 μm (LEμPs). By cutting cross marks on each layer for alignment and positioning, the original two-dimensional (2D) layers were vertically stacked and assembled into a leak-free, multilayered, three-dimensional (3D) architecture composed of two layers of alternating interconnected flow channels. Specifically, the PET surfaces of the first and third layers of the microfluidic module were roughened via laser-engraved pitting to produce the periodic LEμP array. For these two PET layers (i.e., those with LEμPs), the outlet and vertical interconnect accesses (VIAs) were first cut out at designated locations using the normal laser engraving mode. Second, two sections of double-sided tape were cut via laser engraving with patterned fluidic channels to act as the second and fourth layers of the microfluidic module. Third, the PET and double-sided tape layers were cut using laser engraving with large and small inlets, respectively, to act as the fifth and sixth layers of the microfluidic module. These were designed to attach to the skin to collect sweat. These were the final functional layers of the microfluidic module to be processed. Accordingly, all six layers were then etched by laser engraving with cross hollow marks to facilitate vertical stacking and layer-by-layer assembly. Finally, the assembled microfluidics-based sweat loss sensor was trimmed by the laser cutter to form a preset rectangular pattern (1.25 cm × 1.30 cm).

To fabricate a crosstalk-free dual-mode sweat microfluidic system, subsequent integration with the electrochemical module required only additional processing of the top PET layer, as discussed in the next section.

Electrochemical module fabrication

Next, we constructed the electrochemical module. First, a pair of Ag electrodes were thermally evaporated from Cr/Ag (10 nm/150 nm) onto a PET surface covered with a laser-engraved mask pattern. Next, this pair of Ag electrodes were chlorinated into Ag/AgCl electrodes by immersion in a 0.1 mol/L $FeCl_3$ solution for 20 s. Finally, one Ag/AgCl electrode was left as the working electrode for the potentiometric chloride sensor, while the other was coated with 0.8 μL PVB solution to act as the reference electrode. The PVB solution was prepared by dissolving 79.1 mg PVB, 50 mg NaCl, 2 mg F127, and 0.2 mg MWCNTs in 1 mL methanol.

Sensor characterization

The basic performance of the chloride sensors was then characterized by taking open-circuit potential measurements in solutions of 20, 40, 80, and 160 mmol/L NaCl using a CHI 760E electrochemical workstation (CH Instruments, Shanghai, China). Sweat loss sensors were characterized by injecting different flow rates of a NaCl solution using a syringe pump (Longer Precision Pump Co., Ltd., Baoding, China). These results showed that the real-time sweat loss volume could be directly and visually read by the naked eye. Moreover, the sweat rate could be calculated by accounting for the time elapsed. Characterization for dual-mode measurements taken by the integrated system was performed as above for both sensors, which were then operated simultaneously.

Optical reflectance measurements

An ultraviolet–visible (UV/VIS) spectrophotometer with an integrating sphere module (Shimadzu, Japan) enabled diffuse reflectance measurements of microfluidic flow channels with different structures. This included both empty and water-filled channels with LEμPs as well as a channel without LEμPs on PET.

FPCB design

Open-circuit potential (OCP) measurements of the FPCB were achieved using an AD8616ARMZ differential amplifier and an instrumentation amplifier configuration. Specifically, an ultra-low-power microcontroller (STM32F301K8U6) with a built-in 12-bit analog-to-digital converter (ADC) was used to measure the potential difference between the reference and working electrodes and to control the operation of the circuit as a whole. The measured potential signals were then wirelessly transmitted to the computer via a Bluetooth module (BT-11). The FPCB was powered by a small rechargeable Li-ion battery (50 mAh) with an output voltage of 3.7 V. A detailed circuit diagram of the FPCB is shown in Fig. S2 (Supplementary Information).

On-body sweat monitoring during exercise

Constant-load exercise (i.e., cycling at a speed of 15 km/h in the highest resistance gear of a magnetic fitness bike) trials were conducted for three subjects in a room at a constant temperature (25 °C) and relative humidity (about 50% RH). Before sensor or system application, subjects' forearm and abdominal areas were rinsed with deionized water and wiped dry with an electrolyte-free gauze. The integrated system along with the FPCB was then attached to the skin of the subjects using pressure-sensitive double-sided tape. The real-time sweat loss volume could then be visually read and recorded using a mobile phone camera to calculate sweat rate. Chloride concentration data were recorded using computer interface software.

For the reference measurement method, a stacked absorbent patch was prepared by laser-cutting the filter paper (Whatman No. 1, GE Healthcare Life Sciences, Waukesha, USA) to create the same area as covered by the sweat loss sensor (1.625 cm^2). A wound dressing (Tegaderm, 3M, Paul, USA) was then used to fix the absorbent paper to the skin surface of a test site. The number of absorbent paper layers was determined according to the amount of perspiration at the measurement location. In general, placing 12 layers on the abdomen and five tablets on the forearm was able to ensure that they remained unsaturated after 30 min of exercise. Absorbent patches were immediately separated from the skin using clean tweezers after the exercise period; these were then placed in an airtight plastic bag for weighing.

Results

System design for dual-mode sweat monitoring

The sweat microfluidic system comprises two parts: a main microfluidic module for the monitoring of sweat loss and an electrochemical module for chloride sensing. The laser-engraved microfluidic module consists of six layers that were vertically assembled into two nonoverlapping visualizable flow microchannels (Figs. 1a and 1b). The collected sweat can flow forward alternately across these two channels through VIAs, and the user can directly read real-time sweat loss information by noting the position of the sweat front relative to the preset volume markers along the top of the device (Fig. 1c). Here, the width of a single channel is fixed at 500 μm, which corresponds to a volume resolution of 0.5 μL. This provides a trade-off between the module's quantitative capability and the ease of visual observation. As shown in Figs. 1d and 1e, the novel roughening strategy outlined in this paper relies on the laser-engraved pitting mode producing a rough structure composed of a periodic and discontinuous arrangement of LEμPs along the flow channel substrate. This strategy is low-cost and can be used by a wide variety of substrate materials commonly used in microfluidic design, including PET, PI, PEN, and even polydimethylsiloxane (PDMS) (Fig. S1 in Supplementary Information).

The electrochemical module comprises a potentiometric chloride sensor and a matching open-circuit potential measurement FPCB (Fig. 1f and Fig. S2 in Supplementary Information). The chloride sensor is placed above the microfluidic inlet to facilitate real-time detection of fresh sweat. Importantly, this system generates almost no signal crosstalk between the two sweat sensing modes since they are based on two different detection methods, i.e., electrochemical potentiometry and optical colorimetry (see below for details). We also note that the sensor selection for the electrochemical module is not limited to the potentiometric chloride sensor used here. For example, other mass-fabricated electrochemical biosensors would also be suitable for integration in the setup reported here [43–45]. However, the integrated dual-mode sweat monitoring system using the two modules reported here exhibits good overall flexibility and can be comfortably attached to the skin in different areas of the body (Fig. 1g).

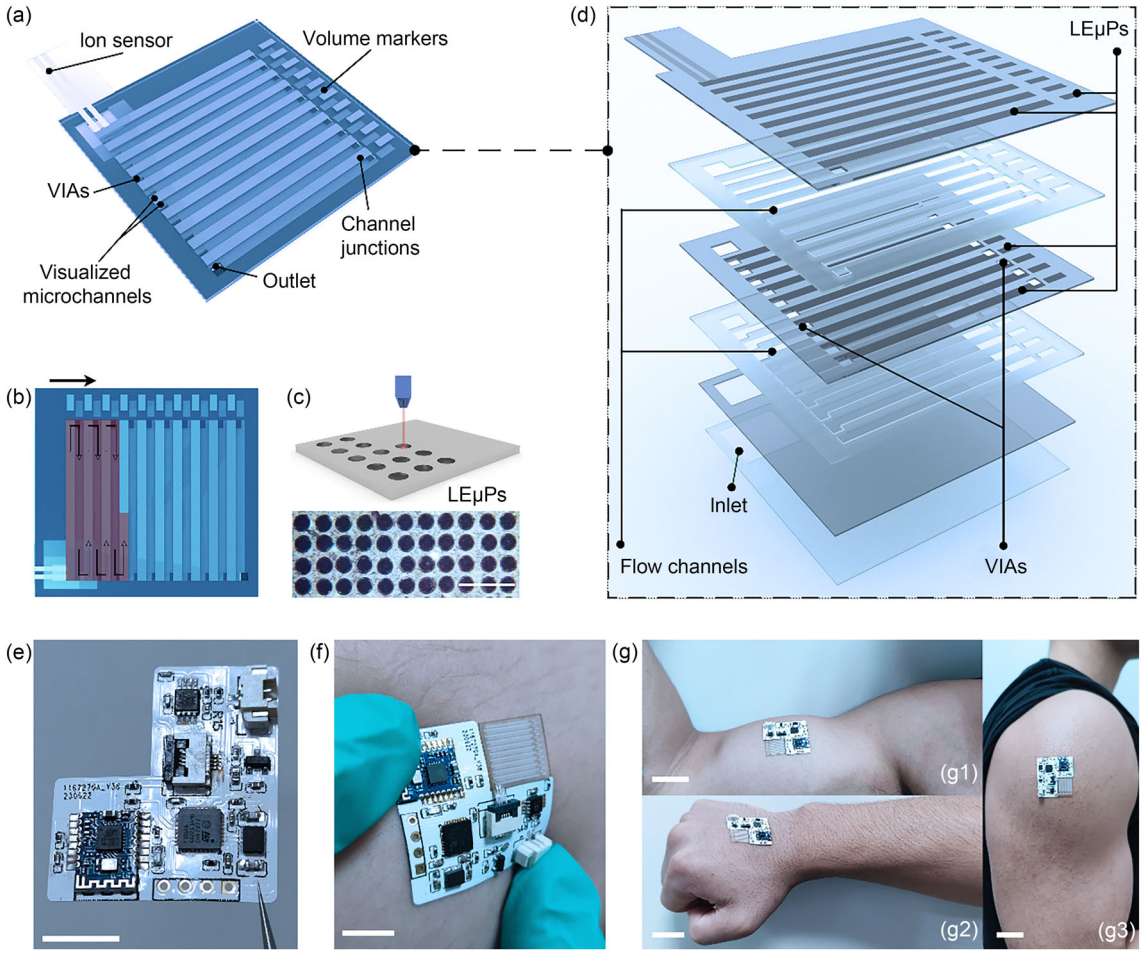

Fig. 1 Schematic of a microfluidic system for dual-mode sweat monitoring. **a**, **b** Structural diagram of the microfluidic system. **c** Illustration showing the flow path of sweat through the microfluidic module and an optical image of LEμPs (scale bar: 100 μm). **d** Illustration showing roughening created using laser-engraved pitting. **e** Photograph of the FPCB (scale bar: 1 cm). **f** Photograph of the integrated system showing its flexibility (scale bar: 1 cm). **g** Photographs of the integrated system when attached to different parts of the arm (scale bar: 1 cm). LEμPs: laser-engraved micropits; FPCB: flexible printed circuit board; VIA: vertical interconnect access

Characterization of the microfluidic module for monitoring sweat loss

The colorimetric microfluidics-based sweat loss sensor was calibrated via syringe pump injection to simulate a wide physiological range of sweat rates (Fig. 2a). Here, real-time sweat volume can be easily determined by visual inspection of the position of the sweat front in the alternating flow channels. The sweat rate can then be obtained by dividing this by the corresponding time elapsed. Here, alternating and vertically interconnected flow channels were assembled from six layers that comprised two types of materials, PET and double-sided tape (Fig. 2b and Fig. S3 in Supplementary Information).

The PET layers on top of each channel were surface-roughened with LEμPs so that they displayed greater reflectivity than the untreated channel. LEμPs on the PET surface were uniformly applied to defined patterned areas by laser ablation (Fig. S4 in Supplementary Information) and showed typical sputter-like pit microstructures (Fig. 2c). Figure 2d shows a cross-sectional image of the microfluidic channel that highlights the contoured geometry of the channel and the VIA of the interconnected junction as well as the LEμPs on the roughened PET surface. Due to these LEμP microstructures, incident light is scattered more strongly at the solid/air interface than at smooth interfaces, which results in a greater proportion of light being reflected (i.e., higher reflectance).

By adjusting the dotting processing time (i.e., from 0.03 to 0.08 ms) in the laser-engraved pitting mode, we fabricated fluidic channels that had different LEμP sizes and depths (Figs. S5 and S6 in Supplementary Information). We then measured their structural reflectance values before and after water filling, and compared these values to smooth fluidic channels without LEμPs (Fig. 2e). Of all variants tested, the

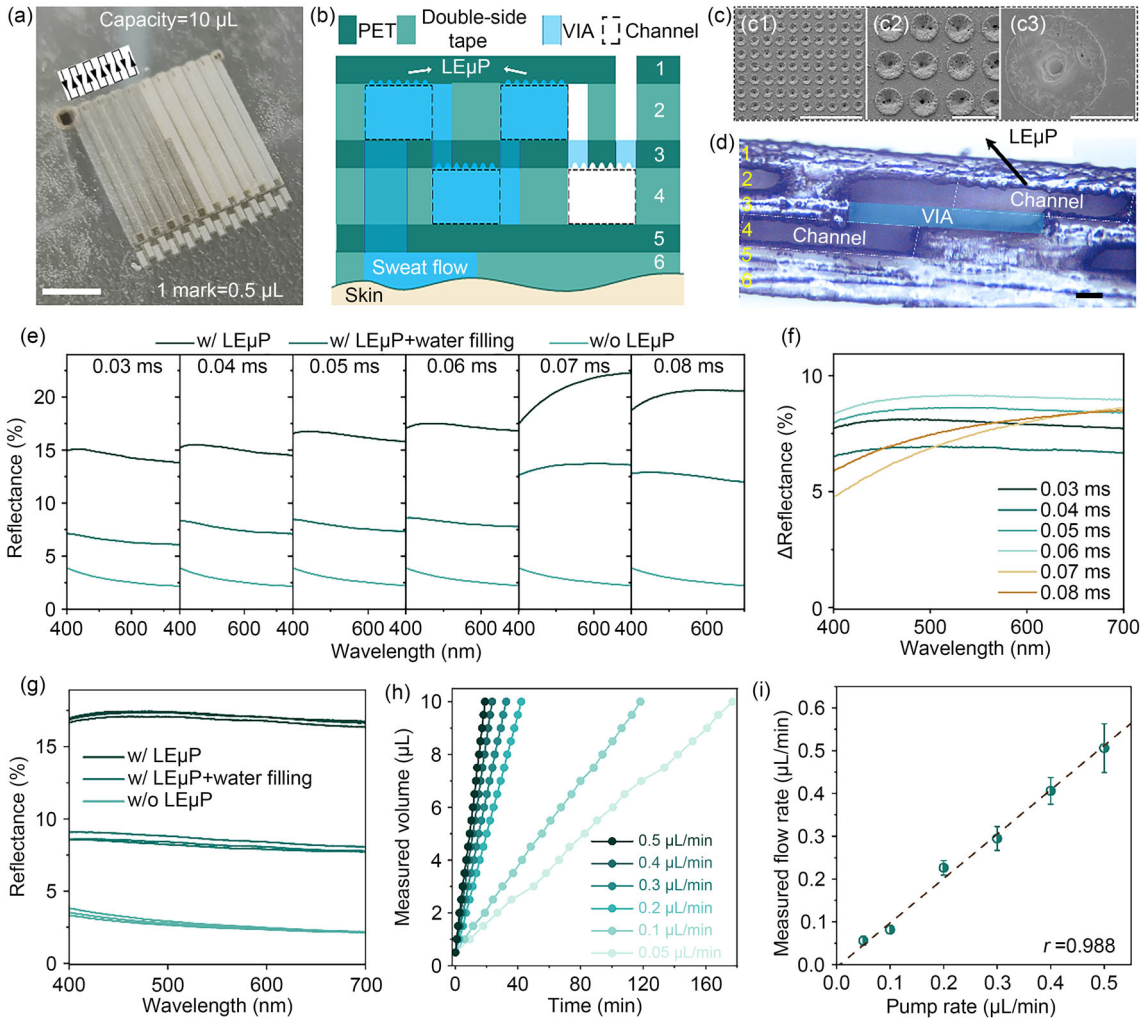

Fig. 2 Schematic and characterization of the microfluidic module for monitoring sweat loss. **a** Photograph of the experimental setup for characterization (scale bar: 0.5 cm). **b** Cross-sectional structural diagram of the microfluidic module. **c** Scanning electron microscope images of LEμPs at different magnifications (scale bars: 200 μm (c1), 50 μm (c2), and 20 μm (c3)). **d** Optical cross-sectional image of the microfluidic device (scale bar: 100 μm). **e** Reflectance comparison of empty and filled channels containing LEμPs, fabricated with different dotting processing time (i.e., ranging from 0.03 to 0.08 ms). **f** Comparison of channel structural reflectance differences before and after water filling. **g** Comparison of the reflectance values of empty and filled channels with and without LEμPs (n=3). **h** Changes in recorded volume marks at different flow rates. **i** The relationship between measured and injected flow rates. Error bars show standard deviation (n=18). r represents a Pearson correlation coefficient. LEμPs: laser-engraved micropits; PET: polyethylene terephthalate; VIA: vertical interconnect access; w/: with; w/o: without

channel with a dotting processing time of 0.06 ms showed the largest reflectance difference before and after water filling (Fig. 2f). Therefore, this optimized laser dotting parameter was used to fabricate subsequent microfluidic modules for the accurate quantification of sweat loss.

As shown in Fig. 2g, larger structural reflectance values enabled the optimized empty channel with LEμPs to diffuse about 17% of incident visible light compared to only about 3% in a similar channel without LEμPs. When sweat flows into the roughened channel and fills the LEμPs, the reflections caused by these microstructures are effectively eliminated due to the similar refractive indices of PET (about 1.6) and sweat (about 1.3) [41]. Moreover, reflectance measurements from three different batches of fluidic channels showed little variation, thereby validating the repeatability of our laser processing method (Fig. 2g). Quantitatively, the roughened channel filled with sweat was found to reflect only about 7% of incident visible light. Therefore, we observed an obvious structural color change visible to the naked eye at the sweat front of the flow channel (Fig. 2a).

For validation, the injected flow rate was set to different values between 0.05 and 0.5 μL/min for the 9 mm^2 sweat collection area to simulate different rates of perspiration during exercise. At a constant (injected) flow rate, the recorded number of volume marks increased linearly with

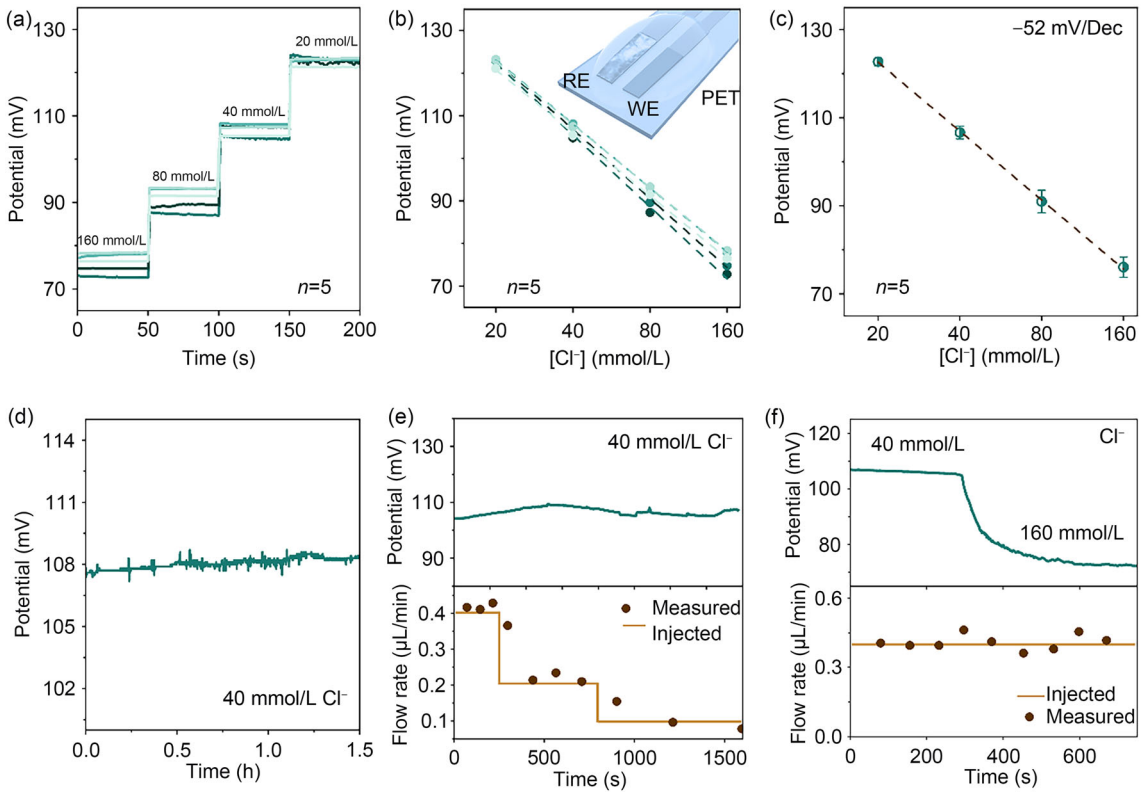

Fig. 3 Characterization of a potentiometric chloride sensor and the crosstalk-free dual-mode measurement of the integrated system. **a**, **b** Chloride sensor performance. Measurements were paused when the testing solution was changed to a new concentration. **c** Curve of the sensor potential response fitted to different chloride concentrations ($[Cl^-]$). Error bars show standard deviation (n=5). **d** Long-term stability of the chloride sensor. **e**, **f** Simultaneous measurement of $[Cl^-]$ and flow rate by varying the injected flow rate and maintaining a constant $[Cl^-]$ concentration (e), as well as by varying $[Cl^-]$ concentration and maintaining a constant injected flow rate (f)

time (Fig. 2h). The measured flow rate can then be obtained by dividing the measured volume by the corresponding time elapsed during the filling of each flow channel. The resulting values calculated for the measured flow rates were consistent with actual values injected by the syringe pump (Fig. 2i). The relatively large measurement error at high flow rates is due to the retardation of the liquid surface tension at the VIA. Finally, we conducted repeated performance characterizations of the six tested flow rates using two microfluidic modules, whose structural color was regenerated after the filled liquid evaporates and reused for the next measurement, thereby demonstrating the reusability of this microfluidic design.

Characterization of the electrochemical module for chloride sensing

Next, we integrated the electrochemical chloride sensing module with the microfluidic system to demonstrate that our design was capable of dual-mode sweat monitoring. The preparation of the chloride sensor is simple, which is conducive to future large-scale and standardized manufacturing of this system. Its operation uses a pair of Ag/AgCl electrodes, one of which is coated with a PVB layer to act as a reference electrode with a stable potential (Fig. S7 in Supplementary Information), while the other is directly used as the chloride-sensitive material [46]. The prepared sensors showed consistent performance in detecting a wide range of physiological chloride concentrations from 20 to 160 mmol/L (Figs. 3a and 3b). For subsequent practical measurements, we fitted the potential response curve of the sensor to chloride concentrations. The equation of the fitted curve is

$$V\,(\mathrm{mV}) = -52.0\,\lg\left(\left[\mathrm{Cl}^-\right]\,(\mathrm{mmol/L})\right) + 190.2,$$

and therefore showed a sensitivity of 52.0 mV/Dec, which is similar to the near-Nernst response behavior (Fig. 3c). Moreover, this chloride sensor showed good long-term stability when used to sense a NaCl solution at a constant concentration (Fig. 3d).

To verify that this dual-mode sweat sensing platform showed no crosstalk, we conducted two subsequent experiments to investigate interactions between colorimetric sweat loss and electrochemical concentration signals when they

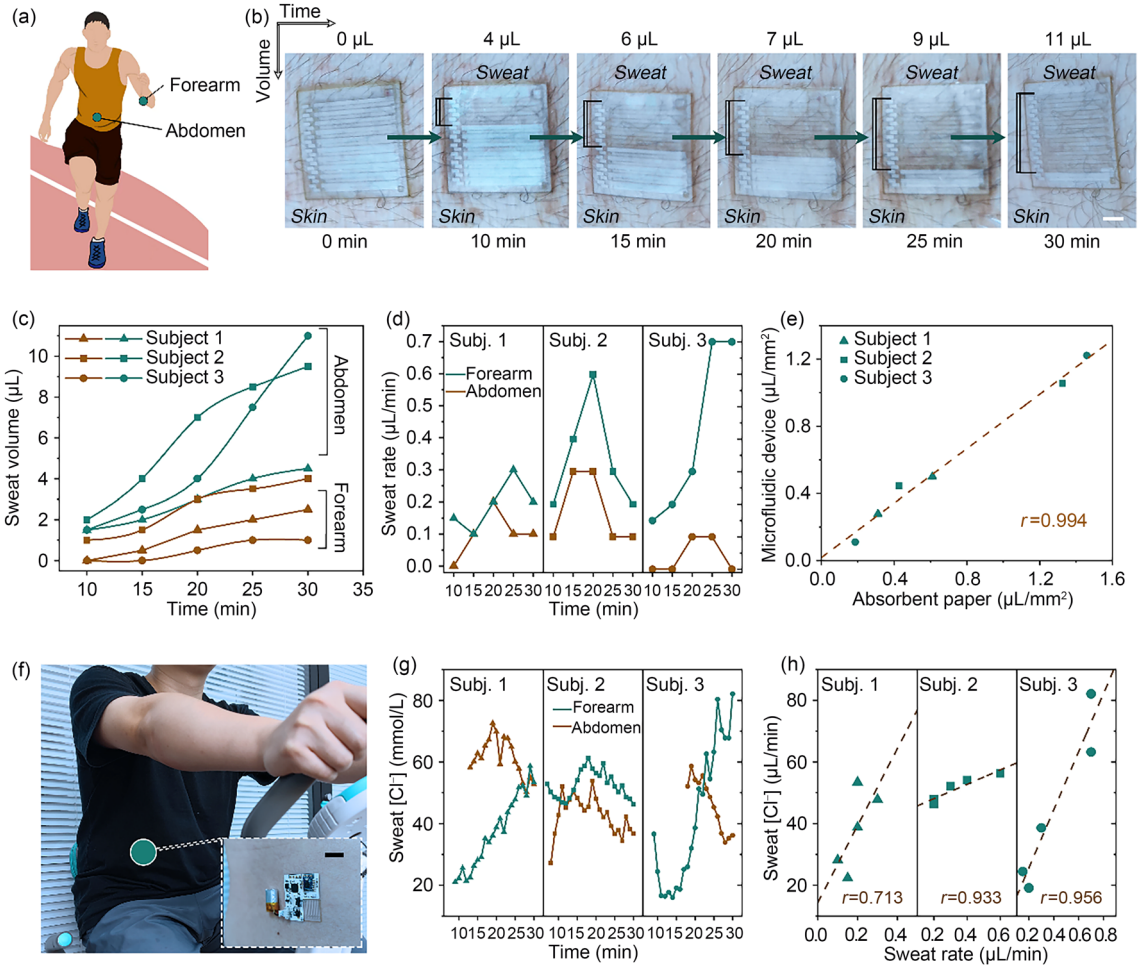

Fig. 4 On-body sweat analysis during exercise. **a** Schematic of the sweat loss sensor attached to two different locations. **b** Photographs of the sensor attached to the abdomen of subject 2 during a standardized exercise treatment used for sweat loss quantification (scale bar: 2 mm). **c**, **d** Comparison of sweat loss volume (c) and rate (d) among three subjects recorded at two different positions. **e** Comparison of sweat loss volumes measured using microfluidic devices and absorbent paper for three subjects. **f** Photograph of the integrated system attached to the abdomen of subject 3 during exercise (scale bar: 1 cm). **g** Changes in sweat [Cl^-] concentrations of the three subjects during exercise. Data were extracted from continuous measurement data at 1-min intervals. **h** Correlations between sweat [Cl^-] levels and sweat loss rates among three subjects. Data were recorded on the abdomen during exercise. *r* represents a Pearson correlation coefficient

were recorded simultaneously. Specifically, the chloride sensor can maintain a stable potential response when the syringe pump is used to vary the flow rate, and this change can also be successfully measured in real time using the sweat loss sensor (Fig. 3e). Similarly, when the concentration of the NaCl was changed suddenly from 40 to 160 mmol/L under a constant flow rate, the flow rate measured by the sweat loss sensor was not affected by this abrupt shift in concentration and tracked the actual injected flow rate well (Fig. 3f). Taken together, these results verified that this dual-mode sweat monitoring system was crosstalk-free.

On-body sweat analysis during exercise

Next, to evaluate the practicality of using our microfluidics-based sweat loss sensor platform, we first recruited three volunteers to ride a fitness bike at a fixed exercise intensity (i.e., maintaining a cycling speed of 15 km/h at the highest resistance gear). During this exercise period, microfluidics-based sweat loss sensors were attached to the abdomens and forearms of subjects to monitor sweat loss differences due to differences in perspiration rates between these two locations (Fig. 4a). As shown in Fig. 4b, the sweat loss volume for the abdomen of subject 2 was recorded in real time by visually reading volume marks corresponding to the sweat filling position. Similarly, the real-time sweat loss volume and the calculated sweat loss rate at two different positions for each of the three subjects during exercise were recorded; these data are shown in Figs. 4c and 4d, respectively. As expected, intraindividual comparisons showed that the sweat loss volume and rate were both higher on the abdomen than

on the forearm, and we also found clear interindividual differences in perspiration ability at the same location. We used the absorbent sweat patch technique [47] as a reference method to simultaneously measure sweat loss in the corresponding area (Fig. S8 in Supplementary Information) to verify the accuracy and reliability of our sensor measurement results. These results showed no differences in sweat loss volumes measured by either technique in any of the subjects (Fig. 4e).

Next, to demonstrate the applicability of the integrated dual-mode sweat sensor platform, we applied sensors to the abdomens and forearms of the three subjects to simultaneously monitor sweat loss and chloride concentration during exercise in real time (Fig. 4f). Each of the subjects read the real-time sweat loss volume and rates directly and visually, while continuously reading the chloride concentration transmitted by the FPCB on a computer (Fig. 4g and Fig. S9 in Supplementary Information). All measured chloride concentrations were within the normal physiological range [13]. More importantly, for all subjects, sweat chloride concentrations were strongly and positively correlated with sweat rates (Fig. 4h), since the reabsorption of chloride ions by the eccrine duct was reduced at high sweat rates [13]. Here, we were also able to detect differences in correlations that corresponded to differences in physical fitness among the three test subjects; our platform is therefore able to detect a considerable degree of interindividual variability [48]. These findings agree with previous investigations [14, 16, 46], and demonstrate the practicality of using the dual-mode sweat sensing capability of this platform, as well as its potential practical value.

Conclusions

In this paper, we propose a novel and universal roughening strategy based on laser-engraved pitting that can be used for various flexible microfluidic substrates. This low-cost strategy is particularly suitable for constructing roughened microfluidics that show obvious reflectance contrasts before and after liquid filling. Based on this idea, we developed a fully laser-engraved microfluidic device for quantifying sweat loss using only the naked eye. The resulting colorimetric sweat loss sensor exhibited a volume resolution of 0.5 μL and a total volume capacity of 11 μL, which is sufficient for daily exercise use. Moreover, this adjustable microfluidic design can be further tailored to meet different performance needs. To demonstrate its effectiveness, we tracked sweat loss in real time on the forearms and abdomens of three test subjects. Furthermore, we developed a crosstalk-free dual-mode sweat microfluidic system that integrates an Ag/AgCl chloride sensor and matching FPCB-based measurements. A pilot on-body sweat analysis using this integrated system demonstrated the utility and commercialization potential of this dual-mode sweat monitoring method for fitness and sports use cases.

Supplementary Information The online version contains supplementary material available at https://doi.org/10.1007/s42242-024-00294-2.

Acknowledgements The authors sincerely acknowledge financial support from the National Natural Science Foundation of China (No. 62174152).

Author contributions BWZ and LLW designed the research and wrote the paper; BWZ, HX, XKQ, LCL, and HLW performed the experiments; BWZ, XKQ, HX, and LLW analyzed the data; BWZ and HLW designed the human studies; HX and LLW revised the paper; LLW supervised the project. All authors substantially contributed to research and reviewed the manuscript.

Declarations

Conflict of interest The authors declare that they have no conflict of interest.

Ethical approval All human subject experiments were conducted in compliance with the ethical standards of the institutional and/or national research committee and with the Declaration of Helsinki of the World Medical Association. The informed consent of all subjects was obtained prior to inclusion in the study.

References

1. Zhong BW, Qin XK, Wang LL (2024) Interindividual- and blood-correlated sweat phenylalanine multimodal analytical biochips for tracking exercise metabolism. Nat Commun 15:624. https://doi.org/10.1038/s41467-024-44751-z
2. Shi YQ, Zhang ZY, Huang QY et al (2023) Wearable sweat biosensors on textiles for health monitoring. J Semicond 44(2):021601. https://doi.org/10.1088/1674-4926/44/2/021601
3. Choi J, Ghaffari R, Baker LB et al (2018) Skin-interfaced systems for sweat collection and analytics. Sci Adv 4(2):eaar3921. https://doi.org/10.1126/sciadv.aar3921
4. Wang JJ, Xu BZ, Zhu YF et al (2023) Microcantilever sensors for biochemical detection. J Semicond 44(2):023105. https://doi.org/10.1088/1674-4926/44/2/023105
5. Emaminejad S, Gao W, Wu E et al (2017) Autonomous sweat extraction and analysis applied to cystic fibrosis and glucose monitoring using a fully integrated wearable platform. Proc Natl Acad Sci USA 114(18):4625–4630. https://doi.org/10.1073/pnas.1701740114
6. Wang B, Zhao CZ, Wang ZQ et al (2022) Wearable aptamer-field-effect transistor sensing system for noninvasive cortisol monitoring. Sci Adv 8(1):eabk0967. https://doi.org/10.1126/sciadv.abk0967
7. Liu XF, Qiu SY, Fang HP et al (2023) A brief review of novel nucleic acid test biosensors and their application prospects for salmonids viral diseases detection. J Semicond 44(2):023103. https://doi.org/10.1088/1674-4926/44/2/023103
8. Zheng JH, Feng CY, Qiu SY et al (2023) Application and prospect of semiconductor biosensors in detection of viral zoonoses. J Semicond 44(2):023102. https://doi.org/10.1088/1674-4926/44/2/023102

9. Sempionatto JR, Lasalde-Ramírez JA, Mahato K et al (2022) Wearable chemical sensors for biomarker discovery in the omics era. Nat Rev Chem 6(12):899–915. https://doi.org/10.1038/s41570-022-00439-w
10. Yang DS, Ghaffari R, Rogers JA (2023) Sweat as a diagnostic biofluid. Science 379(6634):760–761. https://doi.org/10.1126/science.abq5916
11. Zhong BW, Jiang K, Wang LL et al (2022) Wearable sweat loss measuring devices: from the role of sweat loss to advanced mechanisms and designs. Adv Sci 9(1):e2103257. https://doi.org/10.1002/advs.202103257
12. Sonner Z, Wilder E, Heikenfeld J et al (2015) The microfluidics of the eccrine sweat gland, including biomarker partitioning, transport, and biosensing implications. Biomicrofluidics 9(3):031301. https://doi.org/10.1063/1.4921039
13. Baker LB, Wolfe AS (2020) Physiological mechanisms determining eccrine sweat composition. Eur J Appl Physiol 120(4):719–752. https://doi.org/10.1007/s00421-020-04323-7
14. Nyein HYY, Bariya M, Kivimaki L et al (2019) Regional and correlative sweat analysis using high-throughput microfluidic sensing patches toward decoding sweat. Sci Adv 5(8):eaaw9906. https://doi.org/10.1126/sciadv.aaw9906
15. Harshman SW, Strayer KE, Davidson CN et al (2020) Rate normalization for sweat metabolomics biomarker discovery. Talanta 223(Pt 1):121797. https://doi.org/10.1016/j.talanta.2020.121797
16. Baker LB, Model JB, Barnes KA et al (2020) Skin-interfaced microfluidic system with personalized sweating rate and sweat chloride analytics for sports science applications. Sci Adv 6(50):eabe3929. https://doi.org/10.1126/sciadv.abe3929
17. Villiger M, Stoop R, Vetsch T et al (2018) Evaluation and review of body fluids saliva, sweat and tear compared to biochemical hydration assessment markers within blood and urine. Eur J Clin Nutr 72(1):69–76. https://doi.org/10.1038/ejcn.2017.136
18. Liu YCY, Li XF, Yang HL et al (2023) Skin-interfaced superhydrophobic insensible sweat sensors for evaluating body thermoregulation and skin barrier functions. ACS Nano 17(6):5588–5599. https://doi.org/10.1021/acsnano.2c11267
19. Jain V, Ochoa M, Jiang HJ et al (2019) A mass-customizable dermal patch with discrete colorimetric indicators for personalized sweat rate quantification. Microsyst Nanoeng 5(1):29. https://doi.org/10.1038/s41378-019-0067-0
20. Zhao FJ, Bonmarin M, Chen ZC et al (2020) Ultra-simple wearable local sweat volume monitoring patch based on swellable hydrogels. Lab Chip 20(1):168–174. https://doi.org/10.1039/c9lc00911f
21. Parrilla M, Guinovart T, Ferre J et al (2019) A wearable paper-based sweat sensor for human perspiration monitoring. Adv Healthc Mater 8(16):1900342. https://doi.org/10.1002/adhm.201900342
22. Vaquer A, Baron E, de la Rica R (2020) Wearable analytical platform with enzyme-modulated dynamic range for the simultaneous colorimetric detection of sweat volume and sweat biomarkers. ACS Sens 6(1):130–136. https://doi.org/10.1021/acssensors.0c01980
23. Liu MY, Wang SQ, Xiong ZP et al (2023) Perspiration permeable, textile embeddable microfluidic sweat sensor. Biosens Bioelectron 237:115504. https://doi.org/10.1016/j.bios.2023.115504
24. Yuan Z, Hou L, Bariya M et al (2019) A multi-modal sweat sensing patch for cross-verification of sweat rate, total ionic charge, and Na^+ concentration. Lab Chip 19(19):3179–3189. https://doi.org/10.1039/c9lc00598f
25. Nyein HYY, Bariya M, Tran B et al (2021) A wearable patch for continuous analysis of thermoregulatory sweat at rest. Nat Commun 12(1):1823. https://doi.org/10.1038/s41467-021-22109-z
26. Nyein HYY, Tai LC, Ngo QP et al (2018) A wearable microfluidic sensing patch for dynamic sweat secretion analysis. ACS Sens 3(5):944–952. https://doi.org/10.1021/acssensors.7b00961
27. Hourlier-Fargette A, Schon S, Xue YG et al (2020) Skin-interfaced soft microfluidic systems with modular and reusable electronics for in situ capacitive sensing of sweat loss, rate and conductivity. Lab Chip 20(23):4391–4403. https://doi.org/10.1039/d0lc00705f
28. Choi DH, Gonzales M, Kitchen GB et al (2020) A capacitive sweat rate sensor for continuous and real-time monitoring of sweat loss. ACS Sens 5(12):3821–3826. https://doi.org/10.1021/acssensors.0c01219
29. Bariya M, Davis N, Gillan L et al (2022) Resettable microfluidics for broad-range and prolonged sweat rate sensing. ACS Sens 7(4):1156–1164. https://doi.org/10.1021/acssensors.2c00177
30. Wang SQ, Liu MY, Yang XQ et al (2022) An unconventional vertical fluidic-controlled wearable platform for synchronously detecting sweat rate and electrolyte concentration. Biosens Bioelectron 210:114351. https://doi.org/10.1016/j.bios.2022.114351
31. Ghaffari R, Aranyosi AJ, Lee SP et al (2023) The Gx sweat patch for personalized hydration management. Nat Rev Bioeng 1(1):5–7. https://doi.org/10.1038/s44222-022-00005-5
32. Matzeu G, Fay C, Vaillant A et al (2016) A wearable device for monitoring sweat rates via image analysis. IEEE Trans Biomed Eng 63(8):1672–1680. https://doi.org/10.1109/TBME.2015.2477676
33. Liu WY, Cheng HY, Wang XF (2023) Skin-interfaced colorimetric microfluidic devices for on-demand sweat analysis. npj Flex Electron 7(1):43. https://doi.org/10.1038/s41528-023-00275-y
34. Koh A, Kang D, Xue YG et al (2016) A soft, wearable microfluidic device for the capture, storage, and colorimetric sensing of sweat. Sci Transl Med 8(366):366ra165. https://doi.org/10.1126/scitranslmed.aaf2593
35. Reeder JT, Choi J, Xue YG et al (2019) Waterproof, electronics-enabled, epidermal microfluidic devices for sweat collection, biomarker analysis, and thermography in aquatic settings. Sci Adv 5(1):eaau6356. https://doi.org/10.1126/sciadv.aau6356
36. Bandodkar AJ, Gutruf P, Choi J et al (2019) Battery-free, skin-interfaced microfluidic/electronic systems for simultaneous electrochemical, colorimetric, and volumetric analysis of sweat. Sci Adv 5(1):eaav3294. https://doi.org/10.1126/sciadv.aav3294
37. Wu WT, Li LL, Li ZX et al (2023) Extensible integrated system for real-time monitoring of cardiovascular physiological signals and limb health. Adv Mater 35(51):e2304596. https://doi.org/10.1002/adma.202304596
38. Zhang Y, Guo HX, Kim SB et al (2019) Passive sweat collection and colorimetric analysis of biomarkers relevant to kidney disorders using a soft microfluidic system. Lab Chip 19(9):1545–1555. https://doi.org/10.1039/c9lc00103d
39. Wu CH, Ma HJH, Baessler P et al (2023) Skin-interfaced microfluidic systems with spatially engineered 3D fluidics for sweat capture and analysis. Sci Adv 9(18):eadg4272. https://doi.org/10.1126/sciadv.adg4272
40. Qin DT, Gibbons AH, Ito MM et al (2022) Structural colour enhanced microfluidics. Nat Commun 13(1):2281. https://doi.org/10.1038/s41467-022-29956-4
41. Reeder JT, Xue YG, Franklin D et al (2019) Resettable skin interfaced microfluidic sweat collection devices with chemesthetic hydration feedback. Nat Commun 10(1):5513. https://doi.org/10.1038/s41467-019-13431-8
42. Niu PF, Liu YY, Wang XH et al (2022) Darkening of laser-induced graphene in wet for readable in situ real time sweating rate analysis. Adv Mater Interfaces 9(6):2102026. https://doi.org/10.1002/admi.202102026
43. Yang YR, Song Y, Bo XJ et al (2019) A laser-engraved wearable sensor for sensitive detection of uric acid and tyrosine in sweat. Nat Biotechnol 38(2):217–224. https://doi.org/10.1038/s41587-019-0321-x
44. Bi YN, Sun MM, Wang JJ et al (2023) Universal fully integrated wearable sensor arrays for the multiple electrolyte and metabolite monitoring in raw sweat, saliva, or urine. Anal Chem 95(16):6690–6699. https://doi.org/10.1021/acs.analchem.3c00361

45. Min JH, Tu JB, Xu CH et al (2023) Skin-interfaced wearable sweat sensors for precision medicine. Chem Rev 123(8):5049–5138. https://doi.org/10.1021/acs.chemrev.2c00823
46. Xu G, Cheng C, Yuan W et al (2019) Smartphone-based battery-free and flexible electrochemical patch for calcium and chloride ions detections in biofluids. Sens Actuat B 297:126743. https://doi.org/10.1016/j.snb.2019.126743
47. Liu CH, Xu TL, Wang DD et al (2020) The role of sampling in wearable sweat sensors. Talanta 212:120801. https://doi.org/10.1016/j.talanta.2020.120801
48. Eijsvogels TMH, Veltmeijer MTW, Schreuder THA et al (2011) The impact of obesity on physiological responses during prolonged exercise. Int J Obes 35(11):1404–1412. https://doi.org/10.1038/ijo.2010.277

Authors and Affiliations

Bowen Zhong[1,2] · Hao Xu[1,2] · Xiaokun Qin[1,2] · Lingchen Liu[1,2] · Hailong Wang[1,2] · Lili Wang[1,2]

✉ Hao Xu
haoxu19@semi.ac.cn

✉ Lili Wang
liliwang@semi.ac.cn

[1] State Key Laboratory for Superlattices and Microstructures, Institute of Semiconductors, Chinese Academy of Sciences, Beijing 100083, China

[2] Center of Materials Science and Optoelectronic Engineering, University of Chinese Academy of Sciences, Beijing 100049, China